GDCh

Research Articles

Angewandte
Chemie
International Edition
www.angewandte.org

CO₂ Valorization

Light-Assisted CO₂ Hydrogenation over Pd₃Cu@UiO-66 Promoted by Active Sites in Close Proximity

Li-Li Ling, Weijie Yang, Peng Yan, Min Wang, and Hai-Long Jiang*

Abstract: *CO₂ hydrogenation to methanol has attracted great interest while suffering from low conversion and high energy input. Herein, tiny Pd₃Cu nanoparticles are confined into a metal–organic framework (MOF), UiO-66, to afford Pd₃Cu@UiO-66 for CO₂ hydrogenation. Remarkably, it achieves a methanol production rate of 340 μmol g⁻¹ h⁻¹ at 200°C and 1.25 MPa under light irradiation, far surpassing that in the dark. The photo-generated electron transfer from the MOF to antibonding orbitals of CO₂* promotes CO₂ activation and HCOO* formation. In addition, the Pd₃Cu microenvironment plays a critical role in CO₂ hydrogenation. In contrast to the MOF-supported Pd₃Cu (Pd₃Cu/UiO-66), the Pd₃Cu@UiO-66 exhibits a much higher methanol production rate due to the close proximity between CO₂ and H₂ activation sites, which greatly facilitates their interaction and conversion. This work provides a new avenue to the integration of solar and thermal energy for efficient CO₂ hydrogenation under moderate conditions.*

Introduction

The ever-increasing concentration of CO₂ in the atmosphere is resulting in the global warming crisis, which in turn is leading to the search for strategies to achieve CO₂ capture and conversion.[1] Hydrogenation of CO₂ to value-added chemicals is recognized to be a promising way to alleviate of CO₂ emissions.[2] Various kinds of chemicals, such as carbon monoxide (CO), formic acid (HCOOH), methanol (CH₃OH), and methane (CH₄), etc., can be produced in the reaction.[3] Amongst them, methanol is an important chemical feedstock linking the upstream C₁ gaseous small molecules to the downstream bulk chemicals and fuels. It can be easily upgraded via the methanol to olefin/gasoline (MTO or MTG) reaction, which is the so-called "methanol economy".[4]

Accordingly, extensive research efforts have been devoted to the synthesis of methanol by CO₂ hydrogenation in recent decades. Given that the thermodynamically stable

[*] L.-L. Ling, P. Yan, Prof. Dr. H.-L. Jiang
Department of Chemistry
University of Science and Technology of China, Hefei
Anhui 230026 (P.R. China)
E-mail: jianglab@ustc.edu.cn
Homepage: http://staff.ustc.edu.cn/~jianglab/

Dr. W. Yang, M. Wang
School of Energy and Power Engineering
North China Electric Power University
Baoding, Hebei 071003 (P.R. China)

CO₂ molecule involves high C=O bond energy (750 kJ mol⁻¹),[5] the implementation of CO₂ hydrogenation usually requires high energy inputs and appropriate catalysts.[6] The Cu/ZnO-based nanostructures are the most widely used catalysts for this conversion. For instance, the Cu/ZnO/Al₂O₃ catalysts have been industrially applied to achieve gas-phase CO₂ hydrogenation to produce methanol under relatively harsh conditions (usually 50–100 bar, 200–300°C).[7] While elevated temperatures (>240°C) favor CO₂ activation, they are detrimental to methanol production due to the exothermic nature of this reaction and the presence of the competitive reverse water gas shift (RWGS) reaction at higher temperatures.[8] Therefore, it is highly desirable to conduct this reaction under moderate conditions, which not only reduces the energy consumption, but also avoids the side reactions. In addition to thermo-catalytic CO₂ hydrogenation, methanol production can be achieved by electro-catalytic and photocatalytic CO₂ reductions. Although they are conducted under mild conditions, their conversion efficiencies are significantly lower than that of thermo-catalytic processes.[9] In this context, integration of thermo-catalysis and photocatalysis would be a promising way to accelerate CO₂ hydrogenation by introducing inexhaustible light irradiation, i.e., light-assisted CO₂ hydrogenation.[10] Light irradiation is able to reduce the temperature and pressure demand of the thermo-catalytic process, thereby promoting the reaction under moderate conditions.

To this end, it is essential to develop efficient catalysts for the light-assisted CO₂ hydrogenation. A single catalyst incorporating CO₂ and H₂ activation sites, as well as light-harvesting units that work collaboratively, would be desired to promote the reaction. Metal–organic frameworks (MOFs), an emerging class of crystalline porous materials with well-tailorable structures and pore features, would be ideal platforms to fabricate such multifunctional catalyst.[11] Both organic linkers and metal–oxo clusters in the MOF skeleton can behave as active sites and functional units. Moreover, the permanent porosity of MOFs offers inherent conditions to confine guest functional species, particularly metal nanoparticles (NPs),[12] which are favorable to the construction of composite catalysts by integrating their respective functionalities. There have been several studies on thermo-catalytic CO₂ hydrogenation to methanol, based on metal@MOF composites.[13] However, to the best of our knowledge, introducing solar energy to drive thermo-catalytic CO₂ hydrogenation to methanol over MOF-based materials has never been reported yet.

Herein, we incorporate bimetallic Pd₃Cu NPs into a representative metal–organic framework, UiO-66, to afford
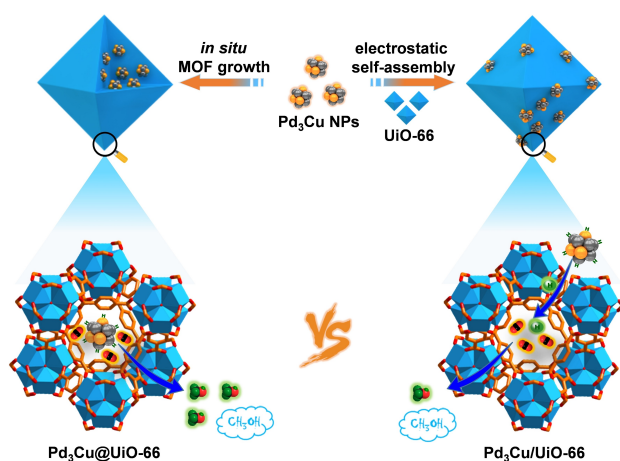
Scheme 1. Schematic illustration showing light-assisted hydrogenation of CO_2 to CH_3OH over $Pd_3Cu@UiO$-66 and Pd_3Cu/UiO-66, of which H_2 and CO_2 molecules are respectively activated on Pd_3Cu NPs and defective Zr–oxo clusters in close proximity in $Pd_3Cu@UiO$-66, leading to its enhanced activity.

$Pd_3Cu@UiO$-66 composites for CO_2 hydrogenation under photo-thermal conditions. The defect sites on the Zr–oxo cluster are able to capture and activate CO_2 molecules. Significantly, the MOF linker harvests solar energy to generate and migrate photo-induced electrons to the Zr–oxo cluster, finally to antibonding orbitals of CO_2^* for the generation of $HCOO^*$ species, accelerating the CO_2 activation. The MOF-confined Pd_3Cu NPs, activating H_2 by a homolytic cleavage mechanism, are in close proximity to the Zr–oxo clusters that activate CO_2 molecules, which greatly promotes the reaction efficiency and affords a methanol production rate of $340\ \mu mol\,g^{-1}\,h^{-1}$, in sharp contrast to $192\ \mu mol\,g^{-1}\,h^{-1}$ for Pd_3Cu supported on UiO-66 (denoted Pd_3Cu/UiO-66), at $200\,°C$ and $1.25\ MPa$ under light irradiation (Scheme 1). Such a high methanol production rate places $Pd_3Cu@UiO$-66 among the best MOF-based catalysts reported for CO_2 hydrogenation (Table S1).
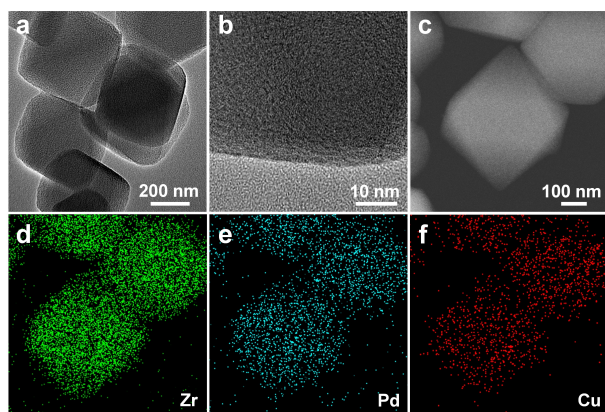
Figure 1. a) Low-magnification and b) high-magnification TEM images of $Pd_3Cu@UiO$-66. c–f) High-angle annular dark-field scanning transmission electron microscopy (HAADF-STEM) and the corresponding Zr, Pd, Cu elemental mapping images.

Results and Discussion

An ultrasound-assisted double-solvent approach (DSA) was adopted to incorporate bimetallic PdCu NPs into the pores of UiO-66 to afford $Pd_xCu@UiO$-66 (x represents Pd/Cu molar ratio in PdCu NPs).[12a,e] The actual contents of Pd and Cu are close to the nominal values, as evaluated by inductively coupled plasma atomic emission spectrometry (ICP-AES) data (Table S2).

Nitrogen sorption reveals a slightly lower surface area of $Pd_xCu@UiO$-66 than the pristine UiO-66, implying that some cavities of UiO-66 might be occupied by the metal NPs (Figure S1). The phase purity and crystallinity of $Pd_xCu@UiO$-66 are evaluated by powder X-ray diffraction (XRD, Figure S2). All the peaks in the XRD patterns are attributed to UiO-66, and no peaks related to Pd or Cu species can be observed. Transmission electron microscopy (TEM) images for $Pd_3Cu@UiO$-66 do not show any observable metal NPs (Figure 1a, b). The energy-dispersive X-ray (EDX) mapping results further support the high dispersion of the metal NPs in the MOF cages (Figure 1c–f). The aforementioned results demonstrate that tiny Pd_3Cu NPs should be well dispersed and successfully confined in the pores of UiO-66.

Encouraged by the ultrafine Pd_3Cu NPs encapsulated into UiO-66, the CO_2 hydrogenation performance of $Pd_3Cu@UiO$-66 composites was evaluated in a stainless-steel experimental setup equipped with a quartz window (Figure S3). It is found that the methanol productivity increases steadily with the increase of temperature (Figure S4). The maximum methanol production rate was achieved at $200\,°C$, with a value of $61\ \mu mol\,g^{-1}\,h^{-1}$. A minor quantity of CO and CH_4 were also detected as gas-phase products. Strikingly, upon introducing light irradiation while fixing other reaction parameters, $Pd_3Cu@UiO$-66 displays a maximum methanol production rate of $340\ \mu mol\,g^{-1}\,h^{-1}$, about 5.6 times higher than that in the dark (Figure 2a). As control, no product can be detected over pristine UiO-66 or in the absence of CO_2. Negligible weight loss in the range of 50–$200\,°C$ and the very stable MOF based on thermogravimetric (TG) analysis exclude the possibility of generating methanol by the MOF decomposition (Figure S5). Moreover, the carbon in the CH_3OH product from CO_2 has been demonstrated by experiments with ^{12}C- and ^{13}C-labeled CO_2/H_2 as feeding gases (Figure S6 and S7). In fact, the reaction clearly gives methanol as the product at different temperatures but not higher than $200\,°C$, with production rates much higher under light irradiation than those in the dark (Figure S8). The methanol selectivity slightly decreases with the increase of the reaction temperature. Such a decrease originates from the competing reverse water gas shift (RWGS) reaction that is difficult to avoid at high temperatures due to its endothermic nature.

The apparent activation energy for CO_2 hydrogenation to methanol is calculated as $48.6\ kJ\,mol^{-1}$ under light irradiation, apparently lower than that in the dark ($61.9\ kJ\,mol^{-1}$) according to the Arrhenius plots (Figure 2b), illustrating that light irradiation might facilitate the activation of CO_2 for the subsequent hydrogenation. Meanwhile,
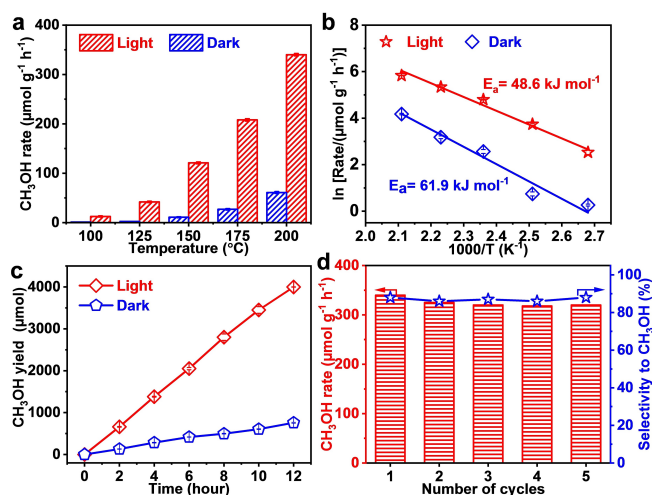
Figure 2. Light-assisted methanol synthesis over Pd$_3$Cu@UiO-66. a) The CH$_3$OH production rate at different reaction temperatures, b) Arrhenius plots and c) temporal profile of CH$_3$OH yield under dark and light conditions. d) Recycling performance under light irradiation.

the kinetic curves manifest that methanol production increases linearly under both light and dark conditions, revealing the good catalytic stability of Pd$_3$Cu@UiO-66 (Figure 2c). The powder XRD profile and TEM images further demonstrate the well retained Pd$_3$Cu NPs and crystallinity of UiO-66 after catalytic reaction (Figure S9, S10). In addition, the activity of Pd$_3$Cu@UiO-66 and the selectivity to methanol remain almost unchanged in five consecutive runs (Figure 2d).

To identify the active sites in Pd$_3$Cu@UiO-66, temperature-programmed desorption (TPD) experiments for CO$_2$ and H$_2$ have been carried out. The CO$_2$-TPD results show that the CO$_2$ desorption peak of Pd$_3$Cu@UiO-66 is very similar to that of UiO-66, indicating the CO$_2$ adsorption might be assignable to the MOF part (Figure 3a). The CO$_2$-TPD profile can be further fitted to two peaks located at 243 and 250 °C. The strong desorption peak at 243 °C might be attributed to the adsorbed CO$_2$ on the two adjacent open Zr^{IV} sites on Zr–oxo cluster. The peak at ∼250 °C is attributed to the desorption of CO$_2$ from the 7-coordinated Zr^{IV} sites that are formed by losing H$_2$O molecules at higher
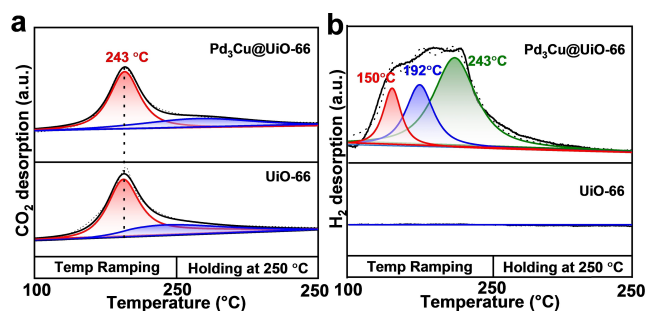

Figure 3. a) CO$_2$-TPD and b) H$_2$-TPD profiles of Pd$_3$Cu@UiO-66 and UiO-66 in the temperature range of 100 to 250 °C.

temperature.[13c,14] These results unambiguously demonstrate that the Zr–oxo cluster is indeed the active site for CO$_2$ adsorption and activation. Furthermore, only one broad signal of H$_2$ desorption is detected in H$_2$-TPD for Pd$_3$Cu@UiO-66, whereas UiO-66 does not give any peak, suggesting that Pd$_3$Cu NPs are the active sites for H$_2$ dissociation (Figure 3b). The peak can be further differentiated into three characteristic peaks, where the peak at ∼150 °C is assigned to H$_2$ desorption on metallic Pd sites,[15] whereas the other two peaks at 192 and 243 °C are attributed to the spillover hydrogen on the Zr–oxo cluster, suggesting that the open sites on the Zr–oxo cluster can accept the spillover hydrogen to form Zr–H species.[13c]

The influence of Pd$_3$Cu loading and Pd/Cu ratio on the efficiency of CO$_2$ hydrogenation has been investigated. The methanol yield increases, while the methanol selectivity almost remains with increased Pd$_3$Cu loadings, suggesting that more dissociated H$_2$ in the reaction does not affect methanol selectivity (Figure S11). The methanol yield exhibits a volcano shape with the increase of Cu content in Pd$_x$Cu@UiO-66 with an optimized Pd/Cu molar ratio at 3 (Figure S12). The result reveals the possible synergistic effect between Pd and Cu species toward H$_2$ activation. The CO adsorption diffuse reflectance infrared Fourier transform spectroscopy (DRIFTs) analysis shows that, the main CO adsorption peak of Pd$_x$Cu@UiO-66 presents an apparent red shift, compared to Pd@UiO-66, which suggests the charge transfer from Cu to Pd (Figure S13).[16] The charge transfer between Pd and Cu has been further confirmed by X-ray photoelectron spectroscopy (XPS). The binding energy of Pd^0 3d$_{5/2}$ in Pd$_3$Cu@UiO-66 is negatively shifted by approximately 0.3 eV, compared to that in Pd@UiO-66 (Figure S14). In the meantime, the binding energy of Cu^0 2p$_{3/2}$ is positively shifted by approximately 0.32 eV compared to that of Cu@UiO-66 (Figure S15). These results jointly support the electron transfer from Cu to Pd in Pd$_3$Cu@UiO-66.[17] Density functional theory (DFT) calculations have been then adopted to illustrate the mechanism for the Pd$_3$Cu alloy effect. The Cu (111), Pd (111) and Pd$_3$Cu (111) are chosen for the slab models (Figure S16–S18). The projected partial density of states (PDOS) analysis uncovers that the Cu alloying leads to an upshift of the Pd d-band center from −1.49 to −1.47 eV (Figure S19, S20).[18] This is in good agreement with the H$_2$ adsorption energy trend over three models of Pd$_3$Cu > Pd > Cu (Figure S21). These results support that the d-band center shifts toward the Fermi level due to the electron transfer from Cu to Pd, thereby boosting the H$_2$ activation by enhancing the interaction between the metal surface and H$_2$.[19]

The reaction over Pd$_3$Cu@UiO-66 has also been conducted under different light intensities. The production rate of methanol linearly increases along with increased light intensity (Figure 4a), reflecting that the reaction might be driven by hot electrons generated via a photochemical process.[20] Moreover, the CH$_3$OH production rate lowers with an increase in the light wavelength (Figure 4b), which is in line with the UV/Vis spectrum of Pd$_3$Cu@UiO-66 (Figure 4c). To unveil the possible mechanism behind the light-assisted CO$_2$ hydrogenation process, electron spin resonance
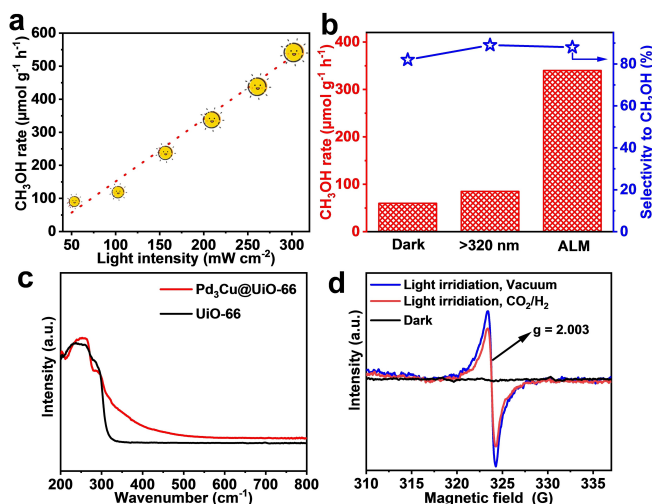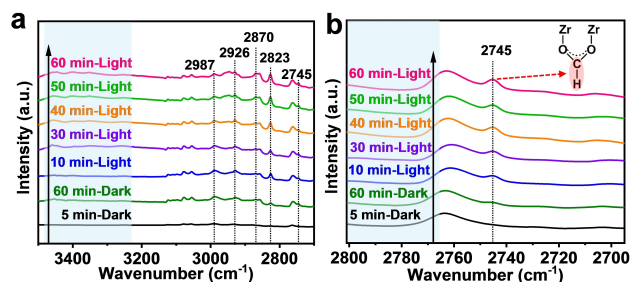
Figure 4. a) Dependence of methanol production rate on light intensity in the presence of Pd₃Cu@UiO-66 catalyst. b) The methanol formation rates over Pd₃Cu@UiO-66 in the dark or under >320 nm or full-spectrum irradiation. c) UV/Vis spectra of UiO-66 and Pd₃Cu@UiO-66. d) ESR spectra of Pd₃Cu@UiO-66 under different conditions.

Figure 5. a) *In situ* DRIFTS spectra of the CO_2 hydrogenation reaction over Pd₃Cu@UiO-66 in the range of 3500–2700 cm⁻¹ shows the formation of diverse surface species. b) The ν(C–H) for bidentate formate species adsorbed on the open Zr sites in the range of 2800–2700 cm⁻¹ (standard conditions: exposure to mixture gas with CO_2/H_2 of 1/3, gas flow rate: 10 mL min⁻¹, 200 °C, 1 bar).

(ESR) tests have been adopted to analyze the electron-transfer process during the reaction. In contrast with the dark conditions, Pd₃Cu@UiO-66 shows a strong ESR peak at g=2.003 under illumination, which could be ascribed to the oxygen-centered active sites in Zr–oxo clusters generated by ligand-to-cluster (LCCT) electron transfer (Figure 4d).[21] Upon introducing CO_2 and H_2, the intensity of the ESR peak decreases slightly, implying an electron transfer from the Zr–oxo cluster to CO_2^* species. Based on the ESR results, it is believed that the linker behaves as an antenna to absorb photons and generates electron-hole pairs, and the photogenerated electrons migrate to the Zr–oxo cluster and finally CO_2 accepts the electrons to be activated.

To further illustrate the reaction mechanism, the surface species evolved during the reaction over Pd₃Cu@UiO-66 have been monitored by *in situ* DRIFT spectra. Upon introducing CO_2/H_2 gas over the catalyst in the dark, the bands at 2987 and 2870 cm⁻¹ are respectively assignable to δ(C–H)+ν_{as}(O–C-O) and ν(C–H) (Figure 5a), which are correlated with HCOO* species. These results reveal that the CO_2 hydrogenation to methanol undergoes a formate pathway in the dark. The peaks at 2926 and 2823 cm⁻¹ might be due to the ν(C–H) modes in the H₃CO* species.[22] Upon light irradiation, the intensity of all surface intermediates substantially increases, suggesting that photo-excitation is able to promote the formation of HCOO* species and accelerate the transformation of HCOO* to other active intermediate species (Figure 5a). Furthermore, the IR peak located at 2745 cm⁻¹ could be assignable to the ν(C–H) vibration from bidentate formate group (*HCOO) adsorbed on the open Zr sites (Figure 5b),[13b] where *HCOO might be formed by the reaction between dissociated H* species from Pd₃Cu and CO_2^* on Zr–oxo cluster, as supported by the H_2/CO_2-TPD results. Overall, the CO_2 hydrogenation to

methanol should follow a formate pathway. The CO_2 molecules adsorbed on the Zr–oxo cluster could accept photo-generated electrons via the ligand-to-cluster charge transfer (LCCT) process under light irradiation, accompanied by the accelerated formation and transformation of HCOO* species to other intermediates and accordingly boosting the conversion of CO_2 to methanol.

The DFT calculations have been executed to verify the reaction pathway. The Zr–oxo SBU with a linker defect is established, in which CO_2 and the reaction intermediate species are adsorbed on two adjacent open Zr sites (Figure 6a). Three major pathways related to HCOO*, COOH* and OCOH* have been evaluated (Figure 6b). The results suggest that the initial hydrogenation of CO_2 on open Zr sites likely proceeds via the formation of the HCOO* intermediate, since HCOO* formation (ΔG=1.61 eV) is kinetically more favorable than COOH* (ΔG=2.36 eV) and
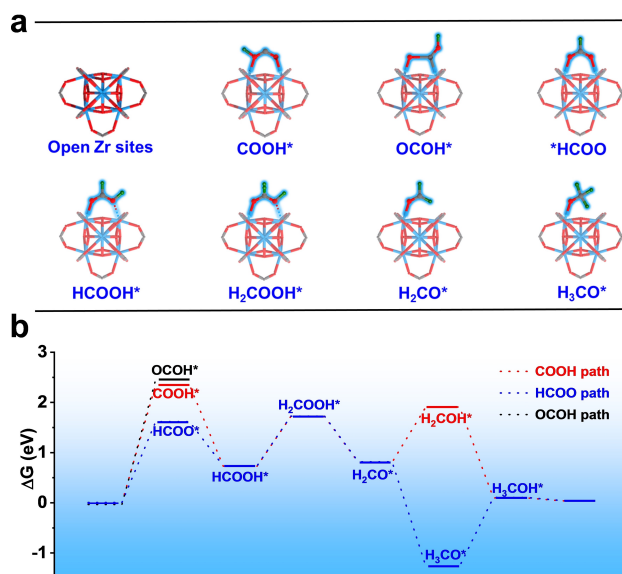
Figure 6. a) Diverse intermediates adsorbed onto an unsaturated Zr–oxo cluster in the catalytic CO_2 hydrogenation. Atom labeling scheme: Zr, cyan; C, brown; O, red; H, green. b) Relative Gibbs energies in potential pathways for CO_2 hydrogenation to CH₃OH.

Angew. Chem. Int. Ed. **2022**, 61, e202116396 (4 of 7)

© 2021 Wiley-VCH GmbH

OCOH* formation ($\Delta G = 2.47$ eV). Therefore, the formation of CH_3OH would be from the HCOO* pathway as the dominating reaction channel, in agreement with the above *in situ* DRIFT results (Figure 5). According to the DFT results, HCOO* is easily hydrogenated into HCOOH*, leading the C–O bond cleavage to form HCO* intermediates, which are finally converted into methanol. Moreover, the formation of HCOO* is identified to be the rate-determining step (RDS) and explained by theoretical calculation with crystal orbital Hamilton population (COHP). Results show that there is more anti-bonding interaction in the Zr–O compounds after the adsorption of HCOO* (Figure S22), which is not favorable to the decrease in system energy, resulting in significant Gibbs free energy change. Note that little change can be observed towards methanol selectivity with the introduction of light irradiation (Figure S4, S8). It is assumed that the catalytic reaction proceeds with a similar pathway under light and dark conditions. The light irradiation accelerates the CO_2 activation, as well as the formation of HCOO* and related intermediates, giving rise to the production of methanol at a faster rate with reduced activation energy.

Remarkably, it is found that the spatial position of Pd_3Cu NPs relative to the MOF particle plays an important role in catalytic efficiency. To deliberately achieve this comparison and guarantee the similar Pd_3Cu sizes and contents, Pd_3Cu NPs in ~3 nm protected by polyvinylpyrrolidone (PVP) were pre-synthesized by a wet-chemical approach and then confined inside or supported on UiO-66, affording $Pd_3Cu_{PVP}@UiO\text{-}66$ and $Pd_3Cu_{PVP}/UiO\text{-}66$, respectively, which can be demonstrated by TEM observation and multiple characterizations (Figure S23–S25, Table S2). The methanol yield of $Pd_3Cu_{PVP}@UiO\text{-}66$ is slightly lower than $Pd_3Cu@UiO\text{-}66$ (Table 1), due to the larger Pd_3Cu size and the negative influence of interface surfactant between Pd_3Cu NPs and the MOF.[23] However, the methanol production rate of $Pd_3Cu_{PVP}@UiO\text{-}66$ is around 1.5-fold higher than that of $Pd_3Cu_{PVP}/UiO\text{-}66$, and much superior to those of the physical mixture of Pd_3Cu_{PVP} NPs and UiO-66 as well as Pd_3Cu_{PVP}/C (Table 1), implying that the microenvironment around Pd_3Cu sites plays a critical role in promoting the conversion.[24] According to the above H_2-TPD results, H_2 first undergoes a dissociation on Pd_3Cu surface and then spillover to the Zr–oxo cluster, and the Pd_3Cu location

might be directly associated with the coverage of dissociated H around Zr–oxo clusters. To verify this, the DRIFT spectra of CO_2/H_2 adsorption indicate that the intensity of some key reaction intermediates, such as HCOO* and H_3CO*, over $Pd_3Cu_{PVP}/UiO\text{-}66$ is much weaker than those of $Pd_3Cu@UiO\text{-}66$ (Figure 5, S26). This suggests that the active sites of Pd_3Cu and Zr–oxo clusters in close proximity greatly facilitate the interaction between dissociated hydrogen and activated CO_2 in the confined pore space of $Pd_3Cu@UiO\text{-}66$, thereby promoting the formation of high-concentration intermediates and boosting the conversion efficiency.[10a]

Since the Zr–oxo clusters in UiO-66 share similar structural features to ZrO_2, which has been demonstrated to be a good support to construct a metal/oxide catalyst for CO_2 hydrogenation to methanol, Pd_3Cu_{PVP}/ZrO_2 was prepared to compare the activity of UiO-66 and ZrO_2 support. In sharp contrast, Pd_3Cu_{PVP}/ZrO_2 displays ~9 and ~13 times lower methanol yield than $Pd_3Cu_{PVP}/UiO\text{-}66$ and $Pd_3Cu_{PVP}@UiO\text{-}66$, respectively (Table 1). The CO_2-TPD of Pd_3Cu_{PVP}/ZrO_2 helps to unveil the mechanism. As expected, the CO_2 desorption signal of Pd_3Cu_{PVP}/ZrO_2 is much weaker than that of $Pd_3Cu_{PVP}/UiO\text{-}66$, suggesting that the active sites for CO_2 adsorption on ZrO_2 are much less than that on the MOF (Figure S27).[22] Similarly, the H_2-TPD signal of Pd_3Cu_{PVP}/ZrO_2 catalysts is also much weaker than that of $Pd_3Cu_{PVP}/UiO\text{-}66$. The H_2-desorption profile can be deconvoluted into two peaks, in which the peak at ~150°C is assigned to H_2 desorption on metallic Pd sites and the peak at 197°C is attributed to the spillover hydrogen on ZrO_2 (Figure S28).[15,25] The CO_2- and H_2-TPD results clearly indicate that the accepting capability for CO_2 and spillover hydrogen on ZrO_2 is much weaker than on the Zr–oxo SBUs of UiO-66. The results highlight that the nanosized metal–oxo clusters in the MOF are able to create more exposed sites for substrates, thereby benefitting their subsequent conversion.[13a]

Conclusion

In summary, ultrafine Pd_3Cu NPs are uniformly encapsulated into UiO-66 to afford $Pd_3Cu@UiO\text{-}66$, which exhibits much enhanced activity in the hydrogenation of CO_2 to methanol by introducing light irradiation. The linkers in UiO-66 can harvest photons to generate charge-separated states. Photo-generated electrons migrate from the linkers to activate CO_2 adsorbed on the unsaturated Zr–oxo clusters. Subsequently, $CO_2^{\bullet-}$ accepts spillover H* from the adjacent Pd_3Cu surface to form the HCOO* intermediate, which is the rate-determining step of the overall reaction. Finally, methanol is formed by the protonation of H_3CO*. As a result, a maximum methanol yield of 340 $\mu mol\,g^{-1}\,h^{-1}$ is achieved under moderate conditions (200°C, 1.25 MPa) and light irradiation, 5.6 times higher than that in the dark. In addition, the Pd_3Cu spatial position relative to the UiO-66 particle plays a critical role in the activity. In contrast to that in $Pd_3Cu/UiO\text{-}66$, the high dispersion Pd_3Cu NPs inside $Pd_3Cu@UiO\text{-}66$ allows the active sites of Zr–oxo clusters and Pd_3Cu NPs in close proximity, enabling a sufficient

Table 1: Light-assisted catalytic selective hydrogenation of CO_2 over different catalysts.[a]

Entry	Catalyst	CH_3OH [$\mu mol\,g^{-1}\,h^{-1}$]
1	$Pd_3Cu@UiO\text{-}66$	340
2	$Pd_3Cu_{PVP}@UiO\text{-}66$	289
3	$Pd_3Cu_{PVP}/UiO\text{-}66$	192
4	Pd_3Cu_{PVP}/ZrO_2	22
5[b]	$Pd_3Cu_{PVP} + UiO\text{-}66$	2.69
6	Pd_3Cu_{PVP}/C	–

[a] Reaction conditions: catalyst (200 mg), 10 mL THF, 1.25 MPa (CO_2: $H_2 = 1:3$), 200°C reaction temperature, light source: 300 W Xe lamp with full-spectral irradiation, light intensity 200 mW cm^{-2}. [b] physical mixture.

supply rate of atomic hydrogen from Pd_3Cu to surrounding Zr–oxo clusters and accelerated RDS with reduced activation energy, which accounts for the significantly enhanced activity. This work not only provides deep insight into the synergistic light and heat utilization, but also demonstrates the significant role of close contact between CO_2 and H_2 activation units in CO_2 hydrogenation.

Acknowledgements

Conflict of Interest

The authors declare no conflict of interest.

Data Availability Statement

The data that support the findings of this study are available from the corresponding author upon reasonable request.

[1] N. Gruber, D. Clement, B. R. Carter, R. A. Feely, S. Heuven, M. Hoppema, M. Ishii, R. M. Key, A. Kozyr, S. K. Lauvset, C. Monaco, J. T. Mathis, A. Murata, A. Olsen, F. F. Perez, C. L. Sabine, T. Tanhua, R. Wanninkhof, *Science* **2019**, *363*, 1193–1199.

[2] P. Gao, S. Li, X. Bu, S. Dang, Z. Liu, H. Wang, S. Zhong, M. Qiu, C. Yang, J. Cai, W. Wei, Y. Sun, *Nat. Chem.* **2017**, *9*, 1019–1024.

[3] a) X. Jiang, X. Nie, X. Guo, C. Song, J. G. Chen, *Chem. Rev.* **2020**, *120*, 7984–8034; b) J. Zhong, X. Yang, Z. Wu, B. Liang, Y. Huang, T. Zhang, *Chem. Soc. Rev.* **2020**, *49*, 1385–1413; c) Z. Wu, H. Wu, W. Cai, Z. Wen, B. Jia, L. Wang, W. Jin, T. Ma, *Angew. Chem. Int. Ed.* **2021**, *60*, 12554–12559; *Angew. Chem.* **2021**, *133*, 12662–12667.

[4] a) P. Tian, Y. Wei, M. Ye, Z. Liu, *ACS Catal.* **2015**, *5*, 1922–1938; b) I. Yarulina, A. D. Chowdhury, F. Meirer, B. M. Weckhuysen, J. Gascon, *Nat. Catal.* **2018**, *1*, 398–411.

[5] L. Liu, S. Wang, H. Huang, Y. Zhang, T. Ma, *Nano Energy* **2020**, *75*, 104959.

[6] a) W. Wang, S. Wang, X. Ma, J. Gong, *Chem. Soc. Rev.* **2011**, *40*, 3703–3727; b) S. Felix, I. Sharafutdinov, F. Abild-Pedersen, C. F. Elkjær, J. S. Hummelshøj, S. Dahl, I. Chorkendorff, J. K. Nørskov, *Nat. Chem.* **2014**, *6*, 320–324; c) S. Kattel, P. J. Ramírez, J. G. Chen, J. Rodriguez, P. Liu, *Science* **2017**, *355*, 1296–1299.

[7] a) A. Beck, M. Zabilskiy, M. A. Newton, O. Safonova, M. G. Willinger, J. A. Bokhoven, *Nat. Catal.* **2021**, *4*, 488–497; b) M. Behrens, F. Studt, I. Kasatkin, S. Kühl, M. Hävecker, F. Abild-Pedersen, S. Zander, F. Girgsdies, P. Kurr, B.-L. Kniep, M. Tovar, R. W. Fischer, J. K. Nørskov, R. Schlög, *Science* **2012**, *336*, 893–897.

[8] a) S. Kuld, M. Thorhauge, H. Falsig, C. F. Elkjær, S. Helveg, I. Chorkendorff, J. Sehested, *Science* **2016**, *352*, 969–974; b) Z.-Q. Wang, Z.-N. Xu, S.-Y. Peng, M.-J. Zhang, G. Lu, Q.-S. Chen, Y. Chen, G.-C. Guo, *ACS Catal.* **2015**, *5*, 4255–4259.

[9] a) W. Zhou, K. Cheng, J. Kang, C. Zhou, V. Subramanian, Q. Zhang, Y. Wang, *Chem. Soc. Rev.* **2019**, *48*, 3193–3228; b) J. Fu, K. Jiang, X. Qiu, J. Yu, M. Liu, *Mater. Today* **2020**, *21*, 897–924; c) H. Jin, C. Guo, X. Liu, J. Liu, A. Vasileff, Y. Jiao, Y. Zheng, S.-Z. Qiao, *Chem. Rev.* **2018**, *118*, 6337–6408; d) Y. Liu, Y. Yang, Q. Sun, Z. Wang, B. Huang, Y. Dai, X. Qin, X. Zhang, *ACS Appl. Mater. Interfaces* **2013**, *5*, 7654–7658.

[10] a) B. Xie, R. Wong, T. Tan, M. Higham, E. K. Gibson, D. Decarolis, J. Calliso, K. F. Aguey-Zinsou, M. Bowker, C. R. A. Catlow, J. Scott, R. Amal, *Nat. Commun.* **2020**, *11*, 1615; b) C. Kim, S. Hyeon, J. Lee, W. Kim, D. C. Lee, J. Kim, H. Lee, *Nat. Commun.* **2018**, *9*, 3027; c) M. Cai, Z. Wu, Z. Li, L. Wang, W. Sun, A. A. Tountas, C. Li, S. Wang, K. Feng, A.-B. Xu, S. Tang, A. Tavasoli, M. Peng, W. Liu, A. S. Helmy, L. He, G. A. Ozin, X. Zhang, *Nat. Energy* **2021**, *6*, 807–814; d) H. Zhang, T. Wang, J. Wang, H. Liu, T. Dao, M. Li, G. Liu, X. Meng, K. Chang, L. Shi, T. Nagao, J. Ye, *Adv. Mater.* **2016**, *28*, 3703–371.

[11] a) H. Furukawa, K. E. Cordova, M. O'Keeffe, O. M. Yaghi, *Science* **2013**, *341*, 1230444; b) M. Ding, R. W. Flaig, H.-L. Jiang, O. M. Yaghi, *Chem. Soc. Rev.* **2019**, *48*, 2783–2828; c) T. Orcid, S. Goswami, Z. Li, A. J. Howarth, O. K. Farha, J. T. Hupp, *Acc. Chem. Res.* **2017**, *50*, 805–813; d) B. Li, H.-M. Wen, Y. Cui, W. Zhou, G. Qian, B. Chen, *Adv. Mater.* **2016**; *28*, 8819–8860; e) X. Zhao, Y. Wang, D.-S. Li, X. Bu, P. Feng, *Adv. Mater.* **2018**, *30*, 1705189; f) E.-X. Chen, M. Qiu, Y.-F. Zhang, Y.-S. Zhu, L.-Y. Liu, Y.-Y. Sun, X. Bu, J. Zhang, Q. Lin, *Adv. Mater.* **2018**, *30*, 1704388.

[12] a) A. Aijaz, A. Karkamkar, Y. J. Choi, N. Tsumori, E. Rönnebro, T. Autrey, H. Shioyama, Q. Xu, *J. Am. Chem. Soc.* **2012**, *134*, 13926–13929; b) G. Lu, S. Li, Z. Guo, O. K. Farha, B. G. Hauser, X. Qi, Y. Wang, X. Wang, S. Han, X. Liu, J. S. DuChene, H. Zhang, Q. Zhang, X. Chen, J. Ma, S. Loo, W. D. Wei, Y. Yang, J. T. Hupp, F. Huo, *Nat. Chem.* **2012**, *4*, 310–316; c) X. Li, T. Goh, L. Li, C. Xiao, Z. Guo, X. Zeng, W. Huang, *ACS Catal.* **2016**, *6*, 3461–3468; d) Q. Yang, Q. Xu, H.-L. Jiang, *Chem. Soc. Rev.* **2017**, *46*, 4774–4808; e) L. Li, Z. Li, W. Yang, Y. Huang, G. Huang, Q. Guan, Y. Dong, J. Lu, S.-H. Yu, H.-L. Jiang, *Chem* **2021**, *7*, 686–698; f) F. Chen, K. Shen, J. Chen, X. Yang, J. Cui, Y. Li, *ACS Cent. Sci.* **2019**, *5*, 176–185; g) G. Li, S. Zhao, Y. Zhang, Z. Tang, *Adv. Mater.* **2018**, *30*, 1800702.

[13] a) B. Rungtaweevoranit, J. Baek, J. R. Araujo, B. S. Archanjo, K. M. Choi, O. M. Yaghi, G. A. Somorjai, *Nano Lett.* **2016**, *16*, 7645–7649; b) E. S. Gutterøda, A. Lazzarinia, T. Fjermestadb, G. Kaura, M. Manzolic, S. Bordigaa, S. Svellea, K. P. Lilleruda, E. Skúlasone, S. Øien-Ødegaarda, A. Novab, U. Olsbyea, *J. Am. Chem. Soc.* **2020**, *142*, 999–1009; c) B. An, J. Zhang, K. Cheng, P. Ji, C. Wang, W. Lin, *J. Am. Chem. Soc.* **2017**, *139*, 3834–3840; d) B. An, Z. Li, Y. Song, J. Zhang, L. Zeng, C. Wang, W. Lin, *Nat. Catal.* **2019**, *2*, 709–717; e) H. Kobayashi, J. M. Taylor, Y. Mitsuka, N. Ogiwara, T. Yamamoto, T. Toriyama, S. Matsumuradef, H. Kitagawa, *Chem. Sci.* **2019**, *10*, 3289–3294.

[14] H. Wu, Y. S. Chua, V. Krungleviciute, M. Tyagi, P. Chen, T. Yildirim, W. Zhou, *J. Am. Chem. Soc.* **2013**, *135*, 10525–10532.

[15] a) R. Prins, *Chem. Rev.* **2012**, *112*, 2714–2738; b) S. H. Pang, J. W. Medlin, *ACS Catal.* **2011**, *1*, 1272–1283.

[16] H. Zhou, X. Yang, L. Li, X. Liu, Y. Huang, X. Pan, A. Wang, J. Li, T. Zhang, *ACS Catal.* **2016**, *6*, 1054–1061.

Angew. Chem. Int. Ed. **2022**, *61*, e202116396 (6 of 7)

© 2021 Wiley-VCH GmbH

[17] a) J. Shan, C. Ye, S. Chen, T. Sun, Y. Jiao, L. Liu, C. Zhu, L. Song, Y. Han, M. Jaroniec, Y. Zhu, Y. Zheng, S.-Z. Qiao, *J. Am. Chem. Soc.* **2021**, *143*, 5201–5211; b) K. Choe, F. Zheng, H. Wang, Y. Yuan, W. Zhao, G. Xue, X. Qiu, M. Ri, X. Shi, Y. Wang, G. Li, Z. Tang, *Angew. Chem. Int. Ed.* **2020**, *59*, 3650–3657; *Angew. Chem.* **2020**, *132*, 3679–3686.

[18] Y. Sun, Z. Xue, Q. Liu, Y. Jia, Y. Li, K. Liu, Y. Lin, M. Liu, G. Li, C.-Y. Su, *Nat. Commun.* **2021**, *12*, 1369.

[19] Q. Fu, Y. Luo, *ACS Catal.* **2013**, *3*, 1245–1252.

[20] Z.-j. Wang, H. Song, H. Pang, Y. Ning, Y. Fang, J. Ye, *Appl. Catal. B* **2019**, *250*, 10–16.

[21] C. Xu, Y. Pan, G. Wan, H. Liu, L. Wang, H. Zhou, S.-H. Yu, H.-L. Jiang, *J. Am. Chem. Soc.* **2019**, *141*, 19110–19117.

[22] J. Wang, G. Li, Z. Li, C. Tang, Z. Feng, H. An, H. Liu, T. Liu, C. Li, *Sci. Adv.* **2017**, *3*, e1701290.

[23] M. Xu, D. Li, K. Sun, L. Jiao, C. Xie, C. Ding, H.-L. Jiang, *Angew. Chem. Int. Ed.* **2021**, *60*, 16372–16376; *Angew. Chem.* **2021**, *133*, 16508–16512.

[24] L. Jiao, J. Wang, H.-L. Jiang, *Acc. Mater. Res.* **2021**, *2*, 327–339.

[25] S. Xia, Z. Yuan, L. Wang, P. Chen, Z. Hou, H.-Y. Chen, S. Tosoni, G. Pacchioni, *ACS Catal.* **2015**, *5*, 5486–5495.